CrossMark

J|M PAPERS

The evolution of a viscous gravity current in a confined geometry

A.J. Hutchinson[1,2,†], **R.J. Gusinow**[1] **and M. Grae Worster**[2]

[1]Department of Computer Science and Applied Mathematics, University of the Witwatersrand, Johannesburg, Wits, 2050, SA

[2]Department of Applied Mathematics and Theoretical Physics, University of Cambridge, Wilberforce Road, Cambridge CB3 0WA, UK

We describe a theoretical and experimental study of an axisymmetric viscous gravity current with a constant flux, confined to the space between two horizontal parallel plates. The effect of confinement results in two regions of flow: an inner region where the fluid is in contact with both plates and an outer annular region where the fluid forms a gravity current along the lower plate. We present a simple theoretical model that describes the flow dynamics by a single dimensionless parameter J, which is the ratio of the characteristic height of an unconfined gravity current to the height of the confined space. Theoretical height profiles display the same characteristics as unconfined gravity currents until $J \approx 0.48$, where a rapid change in behaviour occurs as confinement comes into effect. For larger values of J, the confined viscous gravity current gradually tends to Hele-Shaw flow, with the transition essentially complete by $J \approx 2$. We compare the findings from our theoretical model with the results of a series of experiments using golden syrup with various fluxes and gap spacings. Although the data aligns with the major aspects of the model, it is clear that other physics is at play and a single non-dimensional parameter is not sufficient to capture the flow behaviour fully. We speculate on the factors absent in our model that may be responsible for this mismatch.

Key words: lubrication theory

1. Introduction

Viscous gravity currents, essentially horizontal flows driven by their own buoyancy, have numerous applications in both nature and industry. Unconfined viscous gravity currents

† Email address for correspondence: ah2193@cam.ac.uk

characterise many geophysical flows such as the development of lava domes (Huppert 2006), the spreading of an ice sheet into the ocean (Robison, Huppert & Worster 2010; Schoof & Hewitt 2013) and groundwater flow into a river (Guérin, Devauchelle & Lajeunesse 2014). However, in many settings, vertical confinement can restrict the flow and require an externally imposed pressure gradient in addition to the gravitational force to drive it (see, for example, Nordbotten & Celia 2006). Their study of buoyancy-driven flows in confined porous media and many related studies have been motivated by carbon capture and storage (CCS) technologies, where carbon dioxide can be disposed of by injection into confined aquifers underground, as reviewed by Huppert & Neufeld (2014). A primary question for such confined, gravity-driven flows is the extent to which an injected fluid fills the confining layer. In porous media, it is often found that the flow divides into two regions: the injected fluid can fill the layer completely in the neighbourhood of the source, while further away gravity causes it to flow along just one of the horizontal boundaries. Similar phenomenology is seen in partially confined, layered porous media (Farcas & Woods 2015; Chiapponi *et al.* 2020), the latter including effects of shear-thinning, non-Newtonian rheology.

Comparatively little research has been done to determine the conditions under which free-fluid, viscous gravity currents are impacted by confinement. Such flows have been investigated in two dimensions in the context of filling or cleaning of channels by injection of one viscous fluid to displace another (Taghavi *et al.* 2009; Zheng, Rongy & Stone 2015) and in axisymmetry by Hinton (2020). A review of the effects of confining boundaries on viscous gravity currents has been conducted by Zheng & Stone (2022).

If the ambient fluid is viscous, it can never be completely evacuated from between the invading fluid and the rigid walls and so forms a squeeze film that remains for all time. However, confined, gravity-driven flows may also have important applications in injection moulding, for example, where the ambient fluid (air) can be considered inviscid. Previous studies of injection moulding (Whale *et al.* 1995; Hill 1996) use lubrication theory to study thin-film fluid flow in very narrow confined spaces, in which the effects of gravity are negligible. On the other hand, it has been noted that gravity can play an important role when thicker mouldings are desired (Hoffman 2014).

In this paper, we assume that the ambient fluid is inviscid. In common with flows in porous media, in which the no-slip condition is inapplicable, our model includes a grounding line separating a region in which the injected fluid fills the entire layer, and a region where it only partially fills the layer. Although injection moulding often involves non-Newtonian fluids, we focus here on Newtonian fluids. We also consider an idealised geometry related to injection moulding, namely the flow of a viscous fluid injected from a point source into a narrow, horizontal, air-filled gap starting from some fixed time. In two-dimensional flows in confined porous media (Pegler, Huppert & Neufeld 2014), it has been found that there is a transition from early times at which the injected fluid only partially fills the gap, to late times at which the flow domain has a region close to the source in which the injected fluid fills the gap completely and a region further away in which the injected fluid makes contact with only one of the boundaries. In the case of one viscous fluid displacing another (Taghavi *et al.* 2009; Zheng *et al.* 2015; Hinton 2020), there is a transition in propagation rates from early to late times though, as mentioned above, the ambient fluid cannot be completely evacuated. In the case of axisymmetric spreading of a viscous fluid into an inviscid ambient that we study here, there is a propagating grounding line but the proportion of the flow that makes contact with both boundaries is constant in time and we find a critical dimensionless parameter governing the flow that determines that proportion.
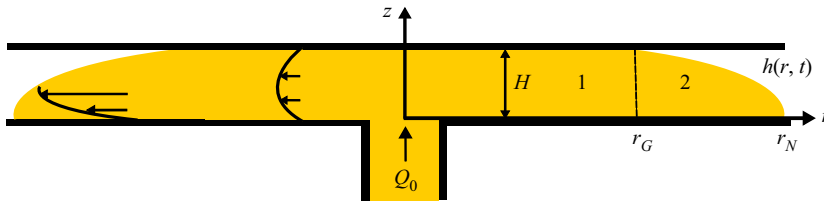
Figure 1. Side view of a confined viscous gravity current. Typical velocity profiles in the inner contact region, $0 < r < r_G(t)$ (Region 1), and the annular gravity current region, $r_G(t) < r < r_N(t)$ (Region 2), are shown.

The paper is outlined as follows. In §2, we present the governing equation for the height profile of the free surface along with the boundary conditions for a confined viscous gravity current. Similarity solutions reduce the governing equation to an ordinary differential equation (ODE) with two free boundaries from which we obtain numerical solutions. We show that the system is described by a single dimensionless parameter J, being the ratio of the scale height for an unconfined viscous gravity current to the gap thickness. Asymptotic solutions are developed for $J \ll 1$ and $J \gg 1$, which help to elucidate the transition from unconfined flow to confined, gravity-driven flow to Hele-Shaw flow. In §3, we describe a series of laboratory experiments using golden syrup designed to test the theory. A discussion of the comparison between theory and experiments and our conclusions are presented in §4.

2. Mathematical model

Consider the axisymmetric propagation of a viscous fluid injected into a small gap of height H between two horizontal parallel plates as illustrated in figure 1. From time $t = 0$, fluid is injected at a constant volume flux Q_0 into the air-filled gap from a small circular hole located on the lower plate. We use a cylindrical coordinate system (r, θ, z), with the origin chosen to coincide with the position of the centre of the source. At later times, two regions of flow develop: an inner contact region, $0 < r < r_G(t)$, where the fluid is in contact with both plates; and an outer annular region, $r_G(t) < r < r_N(t)$, where the free surface of the fluid $z = h(r, t)$ lies below the upper plate. The velocity components in the r and z directions are denoted by $u(r, z, t)$ and $v(r, z, t)$, respectively, and the fluid pressure is given by $p(r, z, t)$. The radial flux, which is continuous across the two regions, is denoted by q. Let ρ be the density of the fluid, and $\nu = \mu/\rho$ the kinematic viscosity, where μ is the dynamic viscosity.

In contrast to the model considered by Hinton (2020), the displaced air is assumed to be inviscid, which allows for the development of a grounding line separating the inner contact region from the outer annular region. We apply lubrication theory, which is valid once $Re(H/L) \ll 1$, where $Re = UH/\nu$ is the Reynolds number and L is the smaller of the characteristic lengths corresponding to r_G and $r_N - r_G$.

In Region 1, $0 < r < r_G(t)$, conservation of mass determines the radial flux q by

$$2\pi r q(r) = Q_0. \tag{2.1}$$

In Region 2, $r_G(t) < r < r_N(t)$, the flow is that of a classical viscous, free-surface gravity current (Huppert 1982) in which the pressure p relative to atmospheric is

$$p(r, z, t) = \rho g(h - z), \tag{2.2}$$

959 A4-3

and the radial velocity

$$u(r, z, t) = \frac{g}{2\nu} \frac{\partial h}{\partial r} z(z - 2h),$$

(2.3)

satisfies no slip at $z = 0$ and no stress at $z = h(r, t)$. The radial flux is given by

$$q(r, t) \equiv \int_0^h u(r, z, t) dz = -\frac{g}{3\nu} h^3 \frac{\partial h}{\partial r}.$$

(2.4)

The rate of change of the free-surface height is related to q by the local mass-conservation equation

$$\frac{\partial h}{\partial t} + \frac{1}{r} \frac{\partial}{\partial r} (rq) = 0,$$

(2.5)

which leads to the equation

$$\frac{\partial h}{\partial t} = \frac{g}{3\nu} \frac{1}{r} \frac{\partial}{\partial r} \left(rh^3 \frac{\partial h}{\partial r} \right).$$

(2.6)

At $r = r_G$, the gravity-current solution intersects the upper boundary so

$$h(r_G(t), t) = H.$$

(2.7)

Additionally, conservation of mass there gives that

$$-\frac{g}{3\nu} h^3 \frac{\partial h}{\partial r} \bigg|_{r_G^+} = \frac{Q_0}{2\pi r_G}.$$

(2.8)

At the leading edge, $r = r_N$, the height of the free surface is zero,

$$h(r_N(t), t) = 0,$$

(2.9)

while global conservation of mass requires that

$$Q_0 t = \pi r_G^2 H + 2\pi \int_{r_G}^{r_N} hr \, dr.$$

(2.10)

Alternatively, we can differentiate (2.10) with respect to time, and use the continuity equation (2.6) with (2.7) and (2.8) to show that

$$\frac{dr_N}{dt} = \lim_{r \to r_N} \frac{q}{h} = \lim_{r \to r_N} \left(-\frac{g}{3\nu} h^2 \frac{\partial h}{\partial r} \right),$$

(2.11)

which is a consequence of imposing zero flux through the leading edge.

2.1. *Similarity solutions*

Classical unconfined axisymmetric Newtonian viscous gravity currents with a constant flux can be described by similarity solutions in which the radius scales with the square root of time and the height scale is independent of time (Huppert 1982). Radial spreading proportional to the square root of time is also a consequence of mass conservation in two-dimensional flow from a point source. It is therefore anticipated that the introduction of the external vertical length scale is consistent with a similar transformation for flows

959 A4-4

confined between parallel, horizontal boundaries. We see this by using H to scale h and balancing the terms in (2.6) to give

$$r \sim \left(\frac{gH^3t}{3\nu} \right)^{1/2}. \tag{2.12}$$

Note that this scaling also balances all three terms in the mass-conservation equation (2.10). We therefore introduce the similarity transformation

$$h(r,t) = Hf(\eta), \quad \eta = \left(\frac{3\nu}{gH^3t} \right)^{1/2} r, \tag{2.13a,b}$$

with

$$r_G(t) = \eta_G \left(\frac{gH^3t}{3\nu} \right)^{1/2}, \quad r_N(t) = \eta_N \left(\frac{gH^3t}{3\nu} \right)^{1/2}, \tag{2.14a,b}$$

where η_G and η_N are constants to be determined. The partial differential equation (2.6) thus reduces to the ODE

$$(\eta f^3 f')' + \tfrac{1}{2}\eta^2 f' = 0, \tag{2.15}$$

and the boundary conditions (2.7)–(2.9) and (2.11) become

$$f(\eta_G) = 1, \quad \eta_G f^3(\eta_G) f'(\eta_G) = -J^4, \tag{2.16a,b}$$

$$f(\eta_N) = 0, \quad \lim_{\eta \to \eta_N} f^2 f' = -\tfrac{1}{2}\eta_N, \tag{2.17a,b}$$

where

$$J = \left(\frac{3Q_0\nu}{2\pi g} \right)^{1/4} \bigg/ H \tag{2.18}$$

is the ratio of the scale height for an unconfined gravity current to the gap width of the cell and $'$ denotes derivatives with respect to η. A similar dimensionless parameter Λ, which reduces to $\Lambda = J^4$ when the density of the ambient fluid is neglected and represents a dimensionless volume flux, was identified by Hinton (2020). Although (2.15) and the boundary conditions at the leading edge (2.17a,b) apply to unconfined axisymmetric gravity currents, the boundary conditions (2.16a,b) are specific to confined flows. We note that the existence of similarity solutions is a consequence of the coincidence mentioned above given axisymmetric flow of a Newtonian fluid in a horizontal layer of uniform thickness. Different relationships between these control parameters would be required for self-similarity if the fluid were non-Newtonian, for example.

From (2.17a,b), we see that the solution for f at η_N is singular. However, an asymptotic solution for f near η_N can be used to discern the behaviour there. Setting $\eta = \eta_N$ in (2.15) results in

$$(f^3 f')' + \tfrac{1}{2}\eta_N f' = 0, \tag{2.19}$$

which, solving subject to (2.17a,b), gives

$$f(\eta) \sim \left(\frac{3\eta_N}{2} \right)^{1/3} (\eta_N - \eta)^{1/3}, \quad f'(\eta) \sim -\left(\frac{\eta_N}{18} \right)^{1/3} (\eta_N - \eta)^{-2/3}. \tag{2.20a,b}$$

This asymptotic solution is used to initialise the numerical solution described in § 2.2.

2.2. *Numerical results*

The second-order ODE (2.15) can be written as a system of first-order ODEs by introducing the variable, $g = \eta f^3 f'$, resulting in

$$f' = \frac{g}{\eta f^3}, \quad g' = -\frac{\eta g}{2f^3}. \tag{2.21a,b}$$

From (2.16a,b) and (2.17a,b), the boundary conditions on f and g are

$$f(\eta_G) = 1, \quad f(\eta_N) = 0, \quad g(\eta_G) = -J^4, \quad g(\eta_N) = 0. \tag{2.22a–d}$$

The routine ODE15s from MATLAB R2019a was used to solve (2.21a,b) subject to (2.22a–d) on the domain $[\eta_G, \eta_N - \delta]$, where $\delta = 10^{-8}$ was chosen such that the solution changed by less than 0.002 % on further reduction of δ. The conditions for f and g at $\eta_N - \delta$,

$$f(\eta) = \left(\frac{3\eta_N}{2}\right)^{1/3} \delta^{1/3}, \quad g(\eta) = -\frac{\eta_N}{3}\left(\frac{3\eta_N}{2}\right)^{4/3} \delta^{1/3}, \tag{2.23a,b}$$

are obtained from the asymptotic solution in (2.20a,b). We used (2.23a,b) as the initial conditions and integrated backwards along the domain $[\eta_G, \eta_N - \delta]$, finding the parameter η_G from the condition $f(\eta_G) = 1$ for a prescribed value of η_N. The corresponding value of J was then determined from (2.22c) as $J = (-g(\eta_G))^{1/4}$. This implicit relationship allowed us to plot $\eta_G(J)$.

Dimensionless height profiles for various values of J are shown in figure 2, each displaying different qualitative features. For $J = 0.25$, the flow is essentially unconfined, the gravity current occupies the majority of the domain, and the inner contact region is negligible. There is a noticeable inflection point near to η_N which is a characteristic of unconfined axisymmetric gravity currents. On the other extreme, for $J = 2$ the inner contact region fills most of the domain, the gravity current occupies little of the domain, and the flow is essentially described as a Hele-Shaw flow. The height profile for an intermediate value of $J = 0.75$ is displayed in figure 2(b) in which both the inner contact region and the gravity current region are well-defined and distinct.

In figure 3(a), the dimensionless front positions, $\eta_G(J)$ and $\eta_N(J)$, are plotted against J, and in figure 3(b) the ratio η_G/η_N is plotted against J. We see that for larger values of J, $\eta_G \approx \eta_N$ and the inner contact region occupies the majority of the domain. The asymptotic behaviour can be determined by using the expression for f in (2.20) and solving for η_G and η_N in terms of J by applying the boundary condition $f(\eta_G) = 1$ and imposing mass-conservation (2.10). Applying $f(\eta_G) = 1$, we find that

$$\eta_N - \eta_G \sim \frac{2}{3\eta_N}, \tag{2.24}$$

while imposing global mass-conservation gives

$$2J^4 \sim \eta_G^2 + 2\int_{\eta_G}^{\eta_N} \eta \left(\frac{3\eta_N}{2}\right)^{1/3} (\eta_N - \eta)^{1/3} \, d\eta$$

$$\sim \eta_G^2 + 2\eta_N \left(\frac{3\eta_N}{2}\right)^{1/3} \int_{\eta_G}^{\eta_N} (\eta_N - \eta)^{1/3} \, d\eta \tag{2.25}$$

to leading order in $\eta_N - \eta_G$. The latter integral in (2.25) is readily calculated and combined with (2.24) to show that

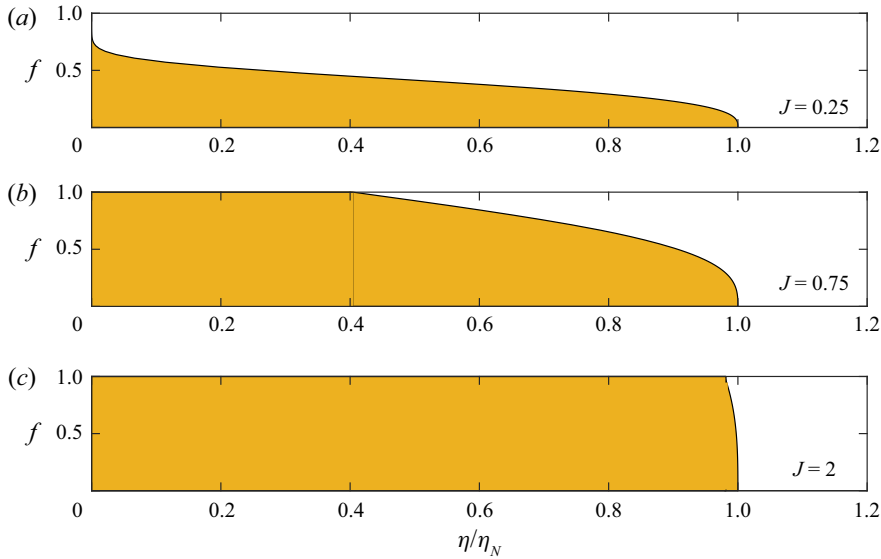$$2J^4 \sim \eta_G^2 + 1. \tag{2.26}$$

Figure 2. Typical dimensionless height profiles determined numerically for different values of J. For small values of J the flow is essentially unconfined, while for large values of J the flow fills the gap almost completely.

From (2.24) and (2.26), we obtain

$$\eta_G \sim \sqrt{2}J^2 \left(1 - \frac{1}{4J^4}\right), \quad \eta_N \sim \sqrt{2}J^2 \left(1 + \frac{1}{12J^4}\right), \tag{2.27}$$

and

$$\frac{\eta_G}{\eta_N} \sim 1 - \frac{1}{3J^4} \tag{2.28}$$

to first order when $J \gg 1$. The leading-order result $\eta_G \sim \eta_N \sim \sqrt{2}J^2$ is straightforwardly understood from conservation of mass in the Hele-Shaw limit. These asymptotic results are seen in figure 3 to give very good representations of the numerical solution once $J \gtrsim 1$. Although there is no grounding line in Hinton's model (Hinton 2020), we can compare the position of the leading edge when the viscosity ratio between the injected fluid and the ambient fluid M tends to infinity. The leading-order position of the leading edge η_N given in figure 6 of Hinton (2020) for $M = 100$ is very close to the value given above, which is to be expected because there will be little ambient fluid remaining in the squeeze film when M is large.

For small values of J, the gravity current is essentially unconfined and the similarity solution derived by Huppert (1982) applies. This can be reproduced here by scaling f with J and η by $J^{3/2}$ and then solving the scaled version of (2.21*a,b*) using the boundary conditions $\eta_G = 0$ and the rescaled $g \to -1$ as $\eta \to 0$. With this approach, our calculations give

$$\eta_N \sim 1.42J^{3/2} \tag{2.29}$$

to leading order, which is equivalent to the results given by Huppert (1982) and Hinton (2020). This asymptotic solution is seen in figure 3(*a*) to agree very closely with the numerical solutions for $J \lesssim 0.75$.
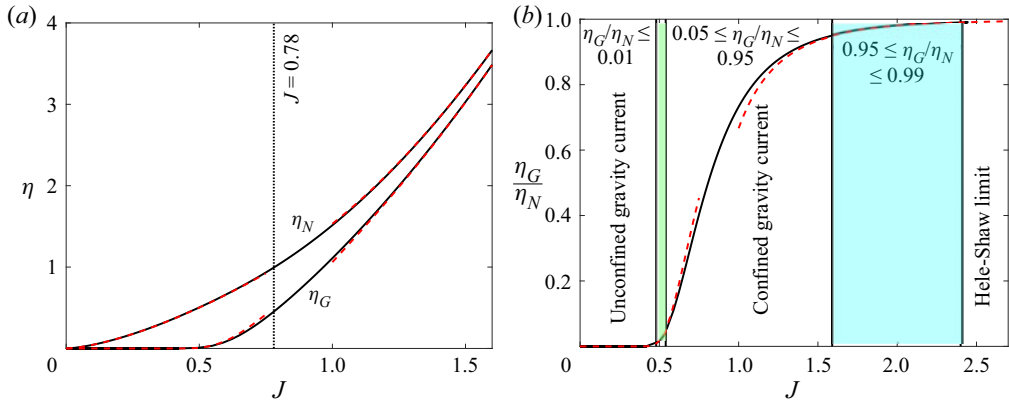
Figure 3. Numerical solutions (black curves) for η_G and η_N against J (*a*) and their ratio (*b*). The associated asymptotic solutions for $J \ll 1$, (2.29) and (2.32), and $J \gg 1$, (2.27) and (2.28), are shown with red, dashed curves. The different flow regimes and the transition regions are shown in (*b*), while in (*a*) the value $J = 0.78$ corresponds to the largest value of J for which the height profiles contain a point of inflection.

We anticipate that $\eta_G \ll 1$ when $J \ll 1$, which is portrayed in figure 3(*a*). Therefore, in the neighbourhood of η_G, the second term in (2.15) is negligible and the equation can then readily be integrated using boundary conditions (2.16*a,b*) to give

$$f \sim \left[1 - 4J^4 \ln \left(\frac{\eta}{\eta_G} \right) \right]^{1/4}. \tag{2.30}$$

We know from scaling that for most of the unconfined current $f = O(J)$ while $\eta = O(J^{3/2})$. Therefore,

$$\eta_G \sim \xi J^{3/2} e^{-1/(4J^4)} \tag{2.31}$$

for some constant ξ. It is noteworthy that the asymptotic solution (2.30) has the property that $f = 0$ at some finite value of η and, if we arbitrarily set that value of η to be η_N, we obtain the result

$$\eta_G \sim \eta_N e^{-1/(4J^4)} \tag{2.32}$$

which coincides with (2.31) with $\xi \simeq 1.42$. We have not been able to prove this result asymptotically but find that it gives excellent agreement with our numerical results, as shown in figure 3. Actually, the coefficient ξ is of minor significance relative to the functional form of (2.31), which shows that η_G behaves in an Arrhenius fashion with J (cf. detonation phenomena) with extremely rapid growth away from zero at a finite value of J. Any reasonable estimate for η_G being significantly above zero (e.g. $\eta_G/\eta_N = 1\%$ or 5 %) gives a transition value of $J \approx 0.5$. This rapid, exponential transition from an unconfined gravity current to a confined current contrasts with the much slower, algebraic transition from confined gravity current to Hele-Shaw flow shown by (2.28) and the shaded regions in figure 3(*b*).

From figure 3(*b*), we see that for $J \leq 0.48$, $\eta_G/\eta_N \leq 0.01$, and the gravity current, which occupies more than 99 % of the domain, is essentially unconfined. For $J \geq 2.40$, $\eta_G/\eta_N \geq 0.99$, and the inner contact region occupies 99 % of the domain, which corresponds to the Hele-Shaw limit. Confined gravity currents form in the interval $0.54 \leq J \leq 1.59$, where the inner contact region occupies between 5 % to 95 % of the domain. Within this region, there is a slight shift in behaviour at $J = 0.78$. For $J < 0.78$, the height profiles contain
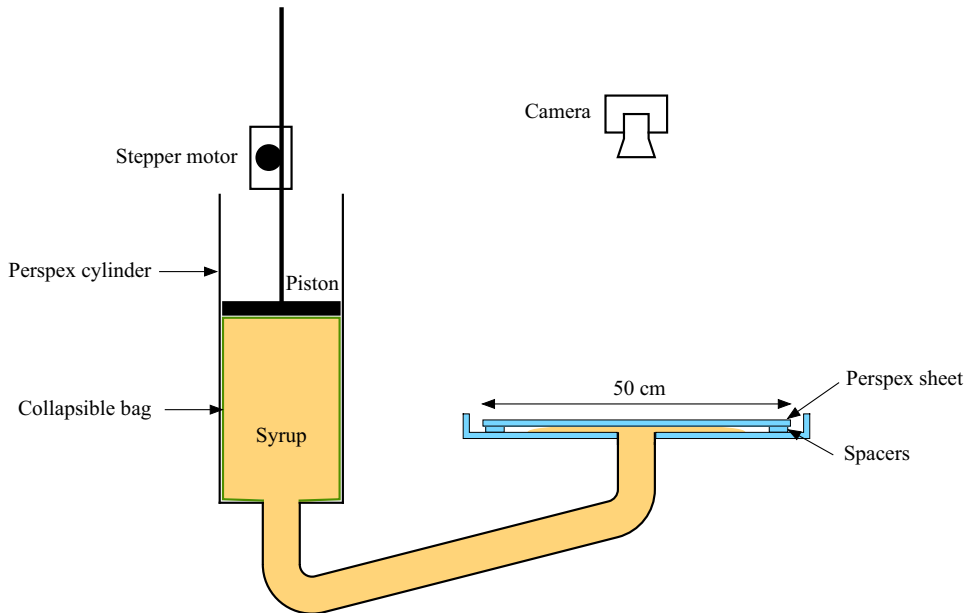
959 A4-8

Figure 4. Schematic diagram of the side view of the experimental set-up drawn approximately to scale showing the delivery system and the narrow gap between two Perspex sheets into which golden syrup is injected.

a point of inflection as shown in figure 2(*a*), whereas for $J > 0.78$ there is no inflection point.

3. Comparison with experiments

We performed a series of 27 experiments in which golden syrup was injected into the narrow gap between two Perspex sheets from a circular hole in the centre of the lower sheet. A schematic diagram of the set-up in shown in figure 4. The length of each side of the top square sheet was 50 cm and the hole in the lower sheet had a diameter of 5.5 cm. Three different gap sizes were investigated for fluxes ranging from 0.06–18 cm^3 s^{-1}. Small square plate spacings were positioned at each of the four corners to support the top sheet. A major consideration in the experimental set-up was the thickness of the top and bottom Perspex sheets, chosen to minimise deflection. The sheets were 1.5 cm thick and were clamped along opposite edges. Given the Young's modulus of Perspex (5.6 GPa), we estimate that these measures ensured that any deflection resulting from the weight of each sheet and the pressure from the fluid that comes into contact with them during an experiment was less than 40 μm in the most extreme experiment. Vernier callipers were used to measure the gap spacing at each of the four corners and at different positions along the outer edges when the top sheet was clamped down firmly. The measured gap spacings were (0.71 ± 0.02) cm, (1.07 ± 0.02) cm and (1.48 ± 0.02) cm. Out of 27 experiments, seven of them were unconfined viscous gravity currents in which the fluid interface did not intersect with the top sheet within the time scale of the experiment. The remaining experiments exhibited confined viscous gravity current behaviour where the inner contact region and the gravity current region were both well-defined, as shown in figure 5(*a*).

The fluid delivery system consisted of a mechanical traverse-driven pump which was used to ensure that the fluid flux remained constant throughout the duration of
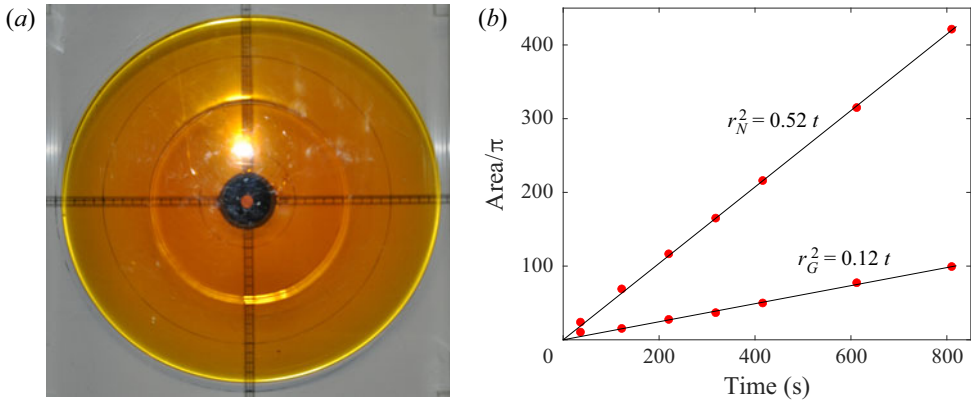
(*a*) (*b*)

Figure 5. Sample photograph of a confined viscous gravity current viewed from above for an experiment with $J = 0.63$ (*a*). Plot of data points for r_G^2 and r_N^2 as well as their linear regressions (*b*).

each experiment. The pump consisted of a vertical cylindrical tube of diameter 19 cm and height 52 cm with a fitted pipe at the bottom end where the fluid is released, and a movable close-fitting piston inside the tube driven by a stepper motor. Inside the cylindrical tube, syrup was contained in a collapsible bag that fed the fluid into the fitted pipe at the bottom end of the tube. Large-diameter pipes were used in the delivery system to reduce viscous resistance and allow the pump to maintain a constant volume flux reliably. The initial position of the piston was set so that it was in direct contact with the top of the sealed end of the bag and that the syrup in the sealed bag expanded to reach the walls of the cylindrical tube. The two input parameters to the controller for the stepper motor were the speed at which the piston is driven downwards, which controls the output flux, and the distance the piston must traverse, which corresponds to the total volume of fluid released.

The relationship between the nominal pump speed S (mm s^{-1}) and the output flux Q (cm^3 s^{-1}) was derived by running a series of Hele-Shaw flow experiments at different piston speeds, and then calculating the volume at various times from the experimental images. A graph of volume versus time was plotted, and the gradient, which is equivalent to the flux, was found for each piston speed. A total of six experiments were used to derive the constant of proportionality between the pump speed and the output flux. The flux values for each experiment are shown in table 1.

The density of the syrup was measured to be (1421 ± 15) kg m^{-3}. Because the viscosity of syrup is highly dependent on temperature T, the temperature of the syrup was recorded before each experiment, and was found to lie in the range 19–21 °C. Using a viscometer, we found that at 22 °C and 23.5 °C the dynamic viscosity of the Lyle's golden syrup that we used was (37.6 ± 1.2) Pa s and (30.3 ± 1.2) Pa s, respectively. In order to estimate the viscosity at lower temperatures in the range 19–21 °C, we first extracted the data set showing dynamic viscosity μ as a function of temperature T for Lyle's golden syrup as presented by Beckett *et al.* (2011) and then applied a curve of the form $\mu = A \exp(-BT)$ to the data set with T measured in Celsius. We found that a best fit gave $A = 1470$ Pa s and $B = 0.15$ °C^{-1}. Using our experimental values, we obtained $\mu = A \exp(-0.15T)$ where $A = 1023$ Pa s. The kinematic viscosity at temperatures 19 °C, 20 °C, 21 °C were then calculated to be (420 ± 30) cm^2 s^{-1}, (360 ± 30) cm^2 s^{-1} and (310 ± 30) cm^2 s^{-1}, respectively. The error corresponds to an uncertainty in temperature of 0.5 °C. The largest source of uncertainty in these experiments was associated with viscosity variations.

959 A4-10

Units	Temp °C	ν cm^2 s^{-1}	H cm	Flux cm^3 s^{-1}	J	α_G	α_N	η_G	η_N	η_G/η_N
Max error	$\pm0.5°$C	9.7 %	2.8 %	1.0 %	5.5 %	2.5 %	2.5 %	11.6 %	11.6 %	23.2 %
	21	310	1.07	0.14	0.36	0.00	0.35	0.00	0.31	0.00
	21	310	1.07	0.30	0.43	0.00	0.49	0.00	0.43	0.00
	19	420	1.07	0.50	0.53	0.20	0.54	0.20	0.55	0.37
	19	420	1.07	0.60	0.55	0.23	0.57	0.24	0.58	0.40
	19	420	1.07	1.00	0.63	0.35	0.72	0.36	0.74	0.49
	20	360	1.07	2.00	0.72	0.51	1.01	0.48	0.96	0.50
	20	360	1.07	2.80	0.78	0.64	1.13	0.61	1.07	0.57
	20	360	1.07	3.50	0.83	0.76	1.23	0.72	1.17	0.62
	20	360	1.07	5.00	0.90	0.95	1.45	0.90	1.38	0.66
	20	360	1.07	6.50	0.97	1.11	1.56	1.05	1.48	0.71
	20	360	1.07	8.00	1.02	1.36	1.79	1.29	1.70	0.76
	21	310	0.71	0.06	0.43	0.00	0.24	0.00	0.39	0.00
	21	310	0.71	0.09	0.48	0.00	0.29	0.00	0.47	0.00
	19	420	0.71	0.10	0.53	0.15	0.27	0.28	0.51	0.56
	21	310	0.71	0.60	0.77	0.44	0.63	0.72	1.03	0.70
	21	310	0.71	1.00	0.88	0.62	0.76	1.01	1.24	0.82
	21	310	0.71	1.50	0.97	0.80	0.95	1.30	1.55	0.84
	21	310	0.71	2.40	1.09	0.92	1.13	1.50	1.84	0.81
	21	310	0.71	4.00	1.24	1.26	1.41	2.05	2.30	0.89
	20	360	1.48	0.10	0.25	0.00	0.30	0.00	0.17	0.00
	21	310	1.48	0.60	0.37	0.00	0.65	0.00	0.35	0.00
	21	310	1.48	1.40	0.46	0.00	0.92	0.00	0.50	0.00
	19	420	1.48	2.00	0.54	0.31	0.93	0.20	0.59	0.33
	19	420	1.48	4.00	0.64	0.54	1.24	0.34	0.78	0.44
	20	360	1.48	8.00	0.74	0.77	1.73	0.45	1.01	0.45
	20	360	1.48	12.00	0.81	1.02	2.04	0.59	1.19	0.50
	21	310	1.48	18.00	0.87	1.23	2.39	0.67	1.29	0.51

Table 1. Experimental input values, which are temperature, kinematic viscosity, gap spacing, and volume flux, along with the corresponding J values found from (2.18). The results for α_G and α_N found from the linear regressions (3.1a,b) as well as η_G, η_N and η_G/η_N obtained from the relationships in (3.2a,b) are displayed. The maximum errors corresponding to each parameter are shown in the third row. The errors shown for η_G, η_N, and η_G/η_N are based on the error estimates reported in earlier columns.

From photographs of the experiments such as that shown in figure 5(a), the mean radius of the inner region $r_G(t)$ and of the outer region $r_N(t)$ were calculated from the areas of ellipses fitted by eye using tools in ImageJ (Schneider, Rasband & Eliceiri 2012) as radius = (area/π)$^{1/2}$. For each data set, we used linear regressions to determine coefficients α_G and α_N such that

$$r_G^2(t) = \alpha_G^2 t, \quad r_N^2(t) = \alpha_N^2 t, \tag{3.1a,b}$$

as shown in figure 5(b). To reduce the influence of initial transients, some early-time data points were omitted from the regression. From (2.14a,b),

$$\eta_G = \alpha_G \left(\frac{3\nu}{gH^3}\right)^{1/2}, \quad \eta_N = \alpha_N \left(\frac{3\nu}{gH^3}\right)^{1/2}. \tag{3.2a,b}$$

The parameters for each experiment and our principal measurements are given in table 1.

In figure 6, the data points (J, η_G) and (J, η_N) are displayed along with the theoretical curves obtained in § 2. The data points $\Box$, $\circ$ and $\diamond$ correspond to gap spacings 0.71 cm, 1.48 cm and 1.07 cm, respectively.
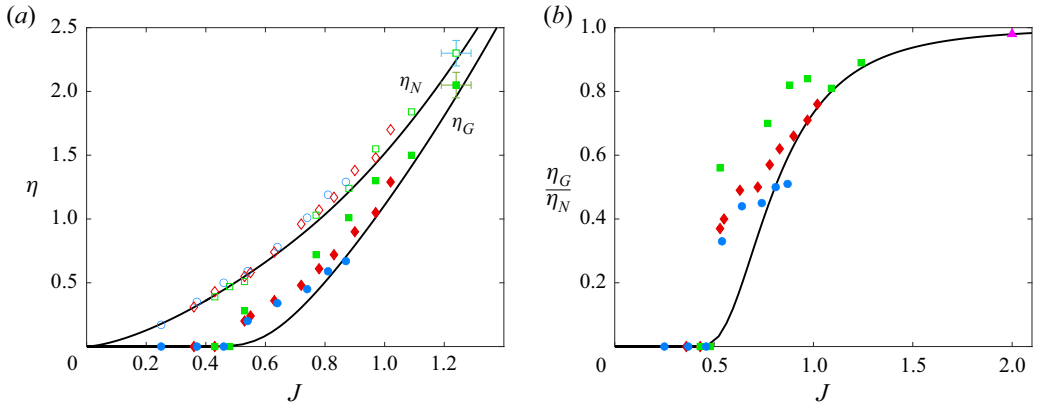
Figure 6. Data points (J, η_G) (filled-in shapes) and (J, η_N) (open shapes), where $\square$, $\circ$ and $\diamond$ correspond to gap spacings 0.71 cm, 1.48 cm and 1.07 cm, respectively, along with the theoretical curves (*a*). Data points $(J, \eta_G/\eta_N)$ (filled-in shapes) along with the theoretical curve (*b*).

Overall, we see that our scaling analysis and corresponding similarity theory capture the dominant variations of η_G and η_N with J very well. There is generally good agreement between our experimental results for η_N, shown by the open symbols in figure 6(*a*), and the corresponding theoretical predictions, particularly given experimental uncertainty, indicated with representative error bars on the right-most data points. There is also reasonable agreement between theory and experiment for the position of the contact line η_N separating the contact region from the gravity current. Here, however, we see some systematic variation of η_G with gap spacing, with the experimental values of η_G corresponding to similar values of J decreasing slightly as the gap spacing increases. Such systematic deviation from the similarity solution and the lack of a complete collapse of the data onto a universal curve given by our scaling suggests the influence of additional physics not included in our model, which we discuss in § 4. We note particularly the increasing deviation of the experimental results and the theoretical predictions as J approaches the values required for essentially unconfined gravity currents from above.

These trends are amplified by considering the ratio η_G/η_N, shown in figure 6(*b*), where we see, nevertheless, that our theory captures the dominant, gradual transition between confined gravity currents and Hele-Shaw flows at values of J around unity very well. A strong result of this study is the rapid transition from essentially unconfined gravity currents to confined currents at values of $J \approx 0.5$ (cf. figures 3*b* and 6*b*). We note that the similarity solution for an axisymmetric gravity current from a point source has a logarithmic singularity at the origin that makes η_G formally non-zero for any non-zero value of J, while laboratory experiments from a finite source allows the current not to make contact with the top plate at all. It is possible that an experiment run for a very long time would eventually have the current make contact with the top plate. However, within the finite time of our experiments, we found that there was no contact for $J < 0.48$ and contact for $J > 0.53$. This compares very favourably with our theoretical predictions that the transition $0.01 < \eta_G/\eta_N < 0.05$ occurs in the range $0.48 < J < 0.54$. Although the annular region was too small for the thin-film approximation to be valid, we show with a pink triangle in figure 6(*b*) the ratio of r_G/r_N for one of the calibration experiments, which coincides with the theoretical curve extremely well.

959 A4-12

4. Discussion and conclusions

We have developed a simple model of the axisymmetric flow of a viscous fluid from a point source into the gap between two horizontal plates and found a family of similarity solutions characterised by a single dimensionless parameter $J = (3Q_0 \nu / 2\pi g)^{1/4}/H$, which is the ratio of the scale height of an unconfined viscous gravity current to the gap width H, where Q_0 is the injected volume flux, ν is the kinematic viscosity of the fluid and g is the acceleration due to gravity. The flow has an inner, pressure-driven region in which the fluid fills the gap and makes contact with both boundaries and an outer, gravity-driven annulus in which the fluid makes contact only with the lower boundary. The proportion of the total flow domain occupied by the inner contact region increases with J.

Our numerical and asymptotic solutions, confirmed by experiment, show that the inner contact region occupies a negligible proportion of the flow domain if J is less than approximately 0.5, around which value there is a rapid, exponential transition towards a confined gravity current in which the contact region occupies a significant proportion of the domain. As J increases further, there is a gradual, algebraic transition to Hele-Shaw flow, with the contact region occupying 99 % of the flow domain once J is greater than approximately 2. In practical terms in relation to injection moulding, this means that, for a given geometry, the injection rate Q_0 must be greater than approximately $0.04\pi g H^4/\nu$ in order for the mould to be filled, and greater than approximately $10\pi g H^4/\nu$ to avoid the influence of gravity. For intermediate values of Q_0, spanning more than two orders of magnitude, wasted excess fluid must be injected in order to ensure complete filling.

Although our model captures the dominant transitions measured in our experiments, we found a systematic deviation between our theoretical predictions and our measurements as the gap width was varied. In particular, the proportion of the flow domain occupied by the inner, contact region increased as the gap width decreased for a fixed value of J. Given that the fluid was injected from a finite source, the theoretical logarithmic singularity associated with a point source does not apply and we saw that the fluid did not make contact with the upper plate at all during the experiments conducted with the smallest values of J. However, once contact was made, the contact line between the inner, contact region and the outer, gravity-driven region advanced further forward than predicted. The fact that our experimental data varies systematically with gap thickness in a way not captured by the scaling of our simple model suggests that other physical mechanisms are at play. One possibility is that hydrodynamic and contact-angle effects akin to those that lead to the teapot effect (Kistler & Scriven 1994) causes the contact line to advance along the upper surface. Another, perhaps in combination, is that once the fluid loses contact with the upper surface there is a rapid transition from a boundary condition of no slip to one of no stress. In common with die swell (Batchelor, Berry & Horsfall 1973) or conditions in the vicinity of grounding lines of marine ice sheets (Schoof 2007; Robison *et al.* 2010), extensional stresses in the fluid film may influence the position of the contact line. Our own visual observations of this contact region were that there is an appreciable meniscus, unlike the glancing contact indicated by the simple theoretical model. These second-order effects on the dynamics of confined viscous currents would make interesting topics for further study.

Author ORCIDs.

ⓘ A.J. Hutchinson https://orcid.org/0000-0002-0585-2371;

ⓘ M. Grae Worster https://orcid.org/0000-0002-9248-2144.

REFERENCES

BATCHELOR, J., BERRY, J.P. & HORSFALL, F. 1973 Die swell in elastic and viscous fluids. *Polymer* **14** (7), 297–299.

BECKETT, F.M., MADER, H.M., PHILLIPS, J.C., RUST, A.C. & WITHAM, F. 2011 An experimental study of low-Reynolds-number exchange flow of two Newtonian fluids in a vertical pipe. *J. Fluid Mech.* **682**, 652–670.

CHIAPPONI, L., PETROLO, D., LENCI, A., DI FEDERICO, V. & LONGO, S. 2020 Dispersion induced by non-Newtonian gravity flow in a layered fracture or formation. *J. Fluid Mech.* **903**, A14.

FARCAS, A. & WOODS, A.W. 2015 Buoyancy-driven dispersion in a layered porous rock. *J. Fluid Mech.* **767**, 226–239.

GUÉRIN, A., DEVAUCHELLE, O. & LAJEUNESSE, E. 2014 Response of a laboratory aquifer to rainfall. *J. Fluid Mech.* **759**, R1.

HILL, D. 1996 Further studies of the injection moulding process. *Appl. Math. Model.* **20** (10), 719–730.

HINTON, E.M. 2020 Axisymmetric viscous flow between two horizontal plates. *Phys. Fluids* **32** (6), 063104.

HOFFMAN, D.A. 2014 Understanding the gravity of the situation. *Plast. Engng Connect.* **70**, 28–31.

HUPPERT, H.E. 1982 The propagation of two-dimensional and axisymmetric viscous gravity currents over a rigid horizontal surface. *J. Fluid Mech.* **121**, 43–58.

HUPPERT, H.E. 2006 Gravity currents: a personal perspective. *J. Fluid Mech.* **554**, 299–322.

HUPPERT, H.E. & NEUFELD, J.A. 2014 The fluid mechanics of carbon dioxide sequestration. *Annu. Rev. Fluid Mech.* **46**, 255–272.

KISTLER, S.F. & SCRIVEN, L.E. 1994 The teapot effect: sheet-forming flows with deflection, wetting and hysteresis. *J. Fluid Mech.* **263**, 19–62.

NORDBOTTEN, J.M. & CELIA, M.A. 2006 Similarity solutions for fluid injection into confined aquifers. *J. Fluid Mech.* **561**, 307–327.

PEGLER, S.S., HUPPERT, H.E. & NEUFELD, J.A. 2014 Fluid injection into a confined porous layer. *J. Fluid Mech.* **745**, 592–620.

ROBISON, R.A.V., HUPPERT, H.E. & WORSTER, M.G. 2010 Dynamics of viscous grounding lines. *J. Fluid Mech.* **648**, 363–380.

SCHNEIDER, C.A., RASBAND, W.S. & ELICEIRI, K.W. 2012 NIH Image to ImageJ: 25 years of image analysis. *Nat. Methods* **9**, 671–675.

SCHOOF, C. 2007 Marine ice-sheet dynamics. Part 1. The case of rapid sliding. *J. Fluid Mech.* **573**, 27–55.

SCHOOF, C. & HEWITT, I. 2013 Ice-sheet dynamics. *Annu. Rev. Fluid Mech.* **45**, 217–239.

TAGHAVI, S.M., SÉON, T., MARTINEZ, D. & FRIGAARD, I. 2009 Buoyancy-dominated displacement flows in near-horizontal channels: the viscous limit. *J. Fluid Mech.* **639**, 1–35.

WHALE, J., FOWKES, N., HOCKING, G. & HILL, D. 1995 A model of the injection moulding process. *J. Aust. Math. Soc.* B **37** (1), 1–15.

ZHENG, Z., RONGY, L. & STONE, H.A. 2015 Viscous fluid injection into a confined channel. *Phys. Fluids* **27** (6), 062105.

ZHENG, Z. & STONE, H.A. 2022 The influence of boundaries on gravity currents and thin films: drainage, confinement, convergence, and deformation effects. *Annu. Rev. Fluid Mech.* **54** (1), 27–56.